Designing Nanoplatelet Alloy/Nafion Catalytic Interface for Optimization of PEMFCs: Performance, Durability, and CO Resistance

Likun Wang,[†] Yuchen Zhou,[†] Janis Timoshenko,[†] Shizhong Liu,[†] Qiao Qiao,[‡] Kim Kisslinger,[§]
Michael Cuiffo,[†] Ya-Chen Chuang,[†] Xianghao Zuo,[†] Yuan Xue,[†] Yichen Guo,[†] Cheng Pan,[†]
Hongfei Li,*[,†] Chang-Yong Nam,[§] Stoyan Bliznakov,[†] Ping Liu,[∥] Anatoly I. Frenkel,[†,∥]
Yimei Zhu,[‡] and Miriam H. Rafailovich*[,†]

[†]Department of Materials Science and Chemical Engineering, State University of New York at Stony Brook, Stony Brook, New York 11794, United States

[‡]Department of Condensed Matter Physics and Materials Science, Brookhaven National Laboratory, Upton, New York 11973, United States

[§]Center for Functional Nanomaterials, Brookhaven National Laboratory, Upton, New York 11973, United States

[∥]Department of Chemistry, Brookhaven National Laboratory, Upton, New York 11973, United States

S Supporting Information

ABSTRACT: We have adapted the two-phase Brust method to synthesize large quantities of AuPd alloy nanoparticles with diameter of 1.86 ± 0.40 nm. When the particles were spread at the air/water interface of a Langmuir−Blodgett (LB) trough, they exhibited a distinct pressure area isotherm curve. The X-ray reflectivity (XRR) shows the formation of an incompressible monolayer with uniform thickness of 1.16 ± 0.02 nm at low pressures which collapses to form a second layer with 2.13 nm thickness at higher pressures. High resolution transmission electron microscopy (HRTEM) imaging of the monolayer indicates that the particles are highly crystalline, with well-defined atomic planes and self-assembly into a hexagonal structure. Extended X-ray absorption fine structure (EXAFS) analysis of the LB lift-off films only shows Au−Au and Au−Pd configurations, consistent with the formation of random alloy rather than

core−shell structure. When the particle monolayer was lifted onto the Nafion membrane of a proton exchange membrane fuel cell (PEMFC), a maximum power output of 0.54 W/cm² was obtained with a Pt loading of only 0.15 and 0.05 mg/cm² at the cathode and anode, respectively. This represents a 15% enhancement, which persists even after 30K cycles, relative to a membrane electrode assembly (MEA) using a noncoated membrane. Density function theory (DFT) modeling of the hexagonally packed platelet nanoparticle alloy structure deposited on Nafion predicted that the SO_3 functionality serves a similar function to metal oxide supports in reducing the activation barrier for the CO oxidation reaction. This was confirmed by measuring the power output of a PEMFC when 0.1% CO was mixed either into the input H_2 stream at the anode or with O_2 at the cathode. In the uncoated MEAs, a significant decrease of 72% and 61% was measured when CO was introduced at the anode and cathode, respectively, while MEAs with coated particle membranes only experienced a decrease of 21% and 17%, respectively. These results indicate that a synergy can be established between the nanoparticle platelets and the surface of the Nafion membrane, which can produce CO resistant PEMFC, that could operate at ambient temperatures on impure, but abundant hydrogen gas such as those produced by reformate or electrolysis processes. The availability of inexpensive H_2 opens opportunities for gas distribution and greatly facilitates the commercialization of PEMFCs, which will conform to the ambitious goals set by the Department of Energy (DOE) for 2020.

KEYWORDS: CO oxidation, AuPd nanoplatelets, alloy/Nafion interface, Langmuir−Blodgett method, PEMFCs
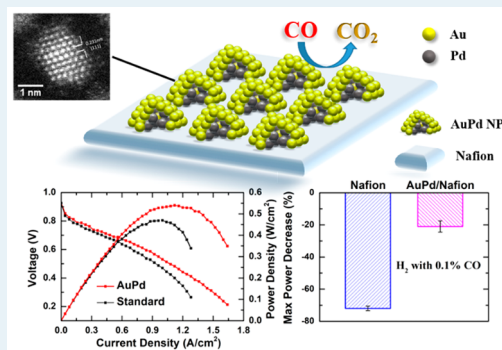
1. INTRODUCTION

Proton exchange membrane fuel cells (PEMFCs) are an area of active research due to their ability to perform at low temperature with relatively high efficiency and provide an environmentally sustainable alternative to fossil fuel power generation.[1−5] However, the major drawback of the technology is the platinum catalyst present at the cathode and anode electrodes.[6−9] Pt is costly and extremely vulnerable to the

poisoning by carbon monoxide, where as little as 25 ppm can reduce its efficiency by nearly 50%.[10,11] CO poisons the Pt catalyst by occupying the catalytic sites through the formations of Pt−CO bonds, which interfere with the Pt−H$_2$ catalysis.[12] To minimize the poisonous effect or event to remove CO, strict PEMFC operation conditions must be obeyed, such as ultrahigh pure hydrogen gas supply and over 100 °C operation temperatures (where the removal of residue CO via oxidation can occur),[13−15] etc. However, both major conditions are unlikely to be satisfied in reality. High purity hydrogen can be generated via electrolysis, where the cost and environmental impact of electricity must be considered.[16,17] Reformate hydrogen, which is far less costly and easily available, is produced predominantly via steam reforming from hydrocarbons with a few percent of CO, as a byproduct via the reaction like $CH_4 + H_2O \rightarrow 3H_2 + CO$.[18] Reduction of CO to ppm level requires multistep purification, which significantly drives up the cost of production.[19−21] Operation of the fuel cell above 100 °C where CO oxidation becomes favorable is also not practical, since it causes dehydration of the Nafion membrane, which is still the most competitive of the commercially available membranes for PEMFCs. The hydration followed by dehydration is shown to produce shape changes in the membrane, which, being confined in the tight space between the gas diffusion layers, exerts complicated stress patterns on the MEA, generating through-plane crack formations and shortening the useful lifetime of the fuel cell.[22]

Fortunately, an alternative solution,[23,24] based on the synergistic effect between metal catalysts and metal oxide supports, has been brought up to enable efficient removal of CO through oxidation at a possibly lower temperature. In this case, the CO oxidation barrier is reduced with promoted catalytic turnover frequency, which eventually accelerates the reaction at the operational temperature range of PEMFCs. For example, Boccuzzi et al.[23] used $^{18}O_2$ and $^{16}O_2$ to demonstrate the reaction pathway of CO oxidation when gas was flowed through the TiO$_2$ substrate coated with Au nanoparticles at room temperature. They emphasized that the oxygen present in the gas reacts with catalytically activated CO anchoring on the borderline of the Au nanoparticles (NPs), which oxidize the CO to CO$_2$. Later other groups demonstrated the generality of this principal to other metal oxide supports including CeO$_2$,[24,25] Al$_2$O$_3$,[26,27] or FeO$_x$.[28,29] Green et al.[30,31] further explained this effect by predicting a construct where the Au NPs were oblate discs whose lattice planes formed stepped interfaces at the contact line with the TiO$_2$ substrate. The direct involvement of the Au−Ti^{4+} dual perimeter sites was proven by the transmission IR spectroscopy data. The interfacial steps serve the perimeter sites for the adsorption of reactant O$_2$ while it is activated as a result of charge transfer from the Au into the antibonding O$_2$, causing di-σ interactions with interfacial Au−Ti^{4+} sites, thereby reducing the activation barrier and facilitating the CO oxidation process. Even though this catalytic pathway has been proven theoretically promising as a solution of the CO problems in PEMFCs, it is relatively difficult to implement since the deposition of the catalyst layers usually requires either even higher temperatures than 100 °C,[32,33] or sophisticated electrochemical procedures,[34,35] which might still damage the Nafion membrane and could not guarantee a uniform platelet film.

In a previous publication,[36] we described a new, facile method for the deposition of a uniform layer of Au nanoplatelets, with adjustable particle spacing, onto Nafion

membrane at room temperature using the Langmuir technique. In the present manuscript we further explore the impact of bimetallic alloy NPs which can potentially be tuned to further increase the enhancement of membrane electrode assembly (MEA) performance. Pd was chosen as the ideal alloying metal component with Au, since we had previously demonstrated that nanoparticle platelets could be produced using the Brust method,[37] and Yan et al.[38] had reported that bimetallic AuPd alloy clusters were even more efficient in the electrocatalysis of the oxygen reduction reaction (ORR) than pure Au or Pd NPs. Here we show that direct contact of AuPd NPs with the Nafion membrane can also provide active catalytic sites for the CO oxidation during fuel cell operation, as described previously for single metal NPs.[36] The results obtained from an MEA with a membrane coated with AuPd alloy NPs using this technique, showed a significant enhancement of the output power, especially when 0.1% CO was added into the hydrogen input stream. DFT calculations suggest the distinct CO oxidation pathway through synergistic interaction of interval optimized AuPd NPs with the SO$_3$ groups on the Nafion side chains, facilitating the oxidation of CO at room temperature. The results establish for the first time the utility of the CO oxidation catalysis model in the operation of hydrogen fuel cells. Furthermore, testing the MEA under controlled temperature, pressure, and humidity conditions indicates that the increased resistance to CO poisoning can translate directly into increased durability of the MEA, as determined under DOE 2020 testing protocols.

2. EXPERIMENTAL SECTION

Materials. All chemicals were analytically pure and used without further purification. Potassium tetrachloroaurate (KAuCl$_4$), potassium tetracholopalladate (K$_2$PdCl$_4$), tetraoctylammonium bromide (TOABr), 1-dodecanethiol, sodium borohydride (NaBH$_4$), toluene, and 2-propanol were all purchased from Sigma-Aldrich. Ethanol was purchased from PHARMCO-AAPER. Nafion 117, Nafion HP, Pt/C (40 wt %), and an electrode of 0.1 mg/cm^2 Pt loading were purchased from Fuel Cell Etc. Nafion ionomer solution (5 wt %) was purchased from Ion Power Inc. H$_2$ (prepurified, 99.99%), O$_2$ (zero grade, 99.8%), N$_2$ (zero grade, 99.998%), and air (dry, 20−22% O$_2$) were purchased from Airgas Inc. The 3% CO in H$_2$ was purchased from Air Liquide (diluted to 0.1% for CO test).

Synthesis of AuPd NPs. AuPd and, for comparison, Au (or Pd) NPs were synthesized through the two-phase method developed by Brust et al.,[37] which has been shown to produce spherical thiol-stabilized particles. This method relies on place exchange kinetics where thiol stabilization and ion agglomeration from the metal salts compete in forming the particles.[39] Since the kinetics are a function of multiple parameters, they can differ for Au and Pd salts, and, hence, the ratio of the two elements in alloy particles is difficult to determine a priori simply from the stoichiometry. We therefore experimented with different ratios of the salts in the synthesis of the alloy particles and then measured the resulting ratio of the elements in the particles. In Figure S1, we plot the performance obtained for the different ratios, where we find that even though the differences between the compositions were small, the 1:1 ratio of the salts in the synthesis (which yielded 2:1 AuPd particles, Table S1) yielded optimal performance and were therefore used exclusively, denoted simply as AuPd NPs unless otherwise specified, in this Article. For the synthesis of AuPd NPs, an

aqueous solution of KAuCl$_4$ and K$_2$PdCl$_4$ (0.55 and 0.55 mmol, respectively; or 1.1 mmol of KAuCl$_4$ for Au NP synthesis, or 1.1 mmol of K$_2$PdCl$_4$ for Pd NP synthesis) in 36 mL of H$_2$O was mixed with a solution of TOABr in toluene (4.8 mmol in 96 mL of toluene). The two-phase mixture was vigorously stirred until all the tetrachloroaurate (AuCl$_4^-$) and tetracholopalladate (PdCl$_4^{2-}$) [or tetrachloroaurate (AuCl$_4^-$), or tetracholopalladate (PdCl$_4^{2-}$)] were transferred into the organic layer. Then 2.0 mmol of 1-dodecanethiol was added into the mixture. A freshly prepared aqueous solution of NaBH$_4$ (12 mmol in 20 mL of water) was added slowly under vigorous stirring; the organic phase at the top layer changed color from orange to deep brown within a few seconds. After stirring for 3 h, the organic phase was separated and evaporated to 5 mL in a rotary evaporator. Then the 5 mL concentrated solution was mixed with 200 mL of ethanol to remove excess thiol, and dark brown precipitate was formed at the bottom after storing in a refrigerator at 4 °C overnight. The precipitate was centrifuged and washed with ethanol three times. It was then dried in a vacuum desiccator for 2 days.

Particle Characterization. The diameter of the particles was measured using dynamic light scattering (DLS), and, assuming a spherical shape, found to be 2.61 ± 1.13 nm for AuPd NPs. The particles were also drop cast on the TEM grid and obtained an average diameter of 2.02 ± 0.56 nm (Figure S2).

The X-ray diffraction (XRD) analysis was performed on powder samples of the synthesized AuPd NPs and, for comparison, Au NPs using a Rigaku Miniflex diffractometer, operating in the Bragg configuration with Cu Kα = 1.54 Å radiation.

X-ray fluorescence (XRF) spectroscopy was performed on a Niton XL3t GOLDD+ hand-held XRF instrument (Thermo scientific) using Niton data Transfer software version 8.4.1.1. All samples were tested in general metals mode to get a more accurate result on the gold and palladium nanoparticles in both atomic percent (atom %). Spectra were analyzed using Niton software version DEV 8.4.1.1.

X-ray Absorption Spectroscopy (XAS) Measurements. For monometallic Au and Pd, and bimetallic AuPd particles, the measurements were performed at ambient conditions in fluorescence mode at Stanford Synchrotron Radiation Light-source (SSRL) beamline BL2-2 in SLAC National Accelerator Laboratory, and Advanced Photon Source (APS) beamline 5-BM in Argonne National Laboratory at L_3-edge of gold (11.9 keV) and K-edge of Pd (24.3 keV). For XAS measurements Langmuir−Blodgett (LB) films were stacked together and fixed with adhesive tape.

AuPd NP Film Fabrication. The NP film was prepared using a KSV 3000 Langmuir−Blodgett trough (KSV Instruments). A 1 mg/mL AuPd NPs in toluene solution was prepared and sonicated for 30 min before use. Nafion membrane was immersed into the water on the LB trough before NP addition. A 200 μL portion of as-prepared NP solution was then carefully spread onto the surface of water by a glass syringe. For the evaporation of toluene solvent, 10 min were used. The barrier moved at a speed of 5 mm/min to compress the NPs on the air/water interface until it reaches the target pressure. Nafion membrane was then lifted at a speed of 2 mm/min by the dipper until the membrane is completely out of the water.

Particle Film Characterization. TEM and energy dispersive X-ray spectroscopy (EDS) analytical data were performed on a JEOL 1400 instrument at an acceleration voltage of 120 kV. High resolution TEM (HRTEM) images were obtained using a JEOL 2100 instrument at 300 kV. X-ray reflectivity (XRR) measurements were performed on a Rigaku Ultima III XRR instrument.

To prepare the cross-sectional TEM sample, AuPd NPs were lifted on a silicon wafer at the surface pressure of 5 mN/m by Langmuir technique first, and then the TEM lamella was prepared using the standard in situ focused ion beam (FIB) lift-out method on the Helios Nanolab 600 instrument with final Ga ion milling performed at 2 keV. The images where the AuPd appears black were acquired in BFTEM (bright field) mode, and images where the particles appear white were acquired in STEM mode with our HAADF detector. The TEM used was the an FEI Talos 200 keV instrument.

Preparation of Catalyst Layer and MEA Fabrication. The homogeneous catalyst ink was prepared by stirring a mixture of Pt/C, Nafion ionomer, and 2-propanol with a mass ratio of 3:2:150. The catalyst ink was air brushed onto the carbon paper with microporous carbon on a hot stage at 90 °C with a Pt loading of 0.15 mg/cm^2 for the cathode and 0.05 mg/cm^2 for the anode. Then the MEA was made by hot-pressing the two carbon papers with Nafion HP membrane with or without coating under the condition of 4 MPa at 130 °C for 1 min.

Evaluation of Single Cell Performance and Durability Test. The single cell performance and durability were evaluated on a fuel cell test station purchased from Fuel Cell Technology, using only Nafion HP membrane. The polarization curves were measured in H$_2$/air atmosphere at 60 °C and 100% relative humidity (RH) under the backpressure of 150 kPa$_{abs}$ with the flow rate stoichiometric ratios being 1.5 and 1.8, respectively. For the calculation of the mass activity, the polarization curves were also measured at 80 °C in H$_2$/O$_2$ atmosphere, 100% RH with the backpressure of 150 kPa$_{abs}$ and stoichiometry being 2 and 9.5, respectively. After the I−V curve was recorded, the cathode was purged with N$_2$. The accelerating stress test (AST) was performed on a potentiostat (Biologic P200) by sweeping potential between 0.6 and 0.9 V at a scan rate of 50 mV/s to investigate the durability of MEAs. The AST measurements were performed in H$_2$/N$_2$ atmosphere at 80 °C, 100% RH, atmospheric pressure, and the H$_2$ flow was fixed at 200 sccm, while the N$_2$ flow was 75 sccm. I−V curves were recorded after different numbers of cycles.

Demonstration PEMFC Kit. The tests described here were conducted using the 16 cm^2 single stack H-TEC EDUCA-TION, GmbH (Luebeck, Germany) F107 Demonstration PEMFC kit, with a specified maximum power output at room temperature of 200 mW. Nafion HP membranes were not stable in this station, and hence only Nafion 117 membranes were used. The membranes were sandwiched between a 16 cm^2 electrode at a Pt loading of 0.1 mg/cm^2 and hydrated by immersion into deionized (DI) water for at least 5 min before assembly. The MEA was press fit together with uniform pressure applied to a four-point screw assembly. The fuel cell test was accomplished using a test station assembled in our laboratory. An electronic load was used to record the performance data. The gas flow rate was controlled by an analogue flow meter which was calibrated relative to a digital flow meter and used to monitor the gas flow speed. The optimum H$_2$ flow rate was first determined and found to be 80 ccm (cm^3/min, 25 °C, 1 atm) regardless of whether the membranes were coated or not.

Computational Method. Vienna ab initio simulation package (VASP)[40−44] with projector augmented wave method[45,46] was used for all the calculations, and the Perdew−Wang functional (GGA-PW91) within the generalized gradient approximation was used to describe exchange-correlation effects. The cutoff energy was 500 eV, and convergences of energy and forces were set to $1 \times 10{-5}$ and 0.01 eV/A, respectively. A γ-point sampling was used for the unit cell. All the atoms in cluster and adsorbates are fully relaxed. The transition states were searched by climbing image nudged elastic band method (NEB) method in VASP (VTST).[47]

3. RESULTS AND DISCUSSION

Formation of Alloy Platelet Particles. The XRD spectra of AuPd and, for comparison, Au NPs, and the determined lattice parameters and crystallite sizes are represented in Figure S3 and Table S2, respectively. The broad peaks corresponding to Au (111) and Pd (111) reflections in the XRD spectra showed that both samples are with a very fine nanocrystalline microstructure. One can see that the maximum of the peak in the AuPd spectra is slightly upshifted in respect of the peak position of the pure Au (111), and the lattice constant obtained, $a = 3.94$ Å, is intermediate between the values of Au and Pd, 4.08 and 3.89 Å, respectively, in agreement with the value obtained by Kaiser for a 2:1 AuPd alloy, where a linear relationship with increasing Au concentration was reported.[48] The crystallite size was calculated from the XRD spectra using the Sherrer equation, and the value calculated, 10.1 Å, indicated that the AuPd nanoparticles consisted of at most two crystallites. This value is consistent with the TEM results, where we obtained an average particle diameter of $D = 2.02 \pm 0.56$ nm, and inspection of the HRTEM images showed that the individual particles are composed of one or two single crystalline orientations.

To confirm the composition of the AuPd NPs we performed XRF analysis. The XRF spectrum of the AuPd NPs powder sample is presented in Figure S4, and the estimated values for the Au and Pd in atom % are summarized in Table S3. The XRF results showed that the atomic ratio between Au and Pd in the AuPd NP samples of interest is 62:37 which is close to 2:1, and in agreement with our findings from the TEM−EDS analysis.

The pressure−area isotherm curve obtained when a solution of AuPd NPs was spread at the air/water interface on a Langmuir−Blodgett trough is shown in Figure 1. A schematic
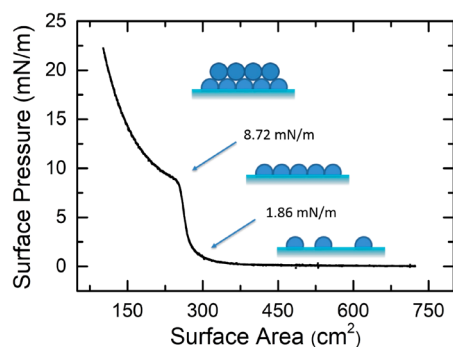

Figure 1. Isothermal curve for thiol-stabilized AuPd NPs. Schemes of the particle distribution corresponding to different sections of the pressure/area curve are presented.

of the particle arrangement corresponding to the reported surface pressures, as deduced from the TEM images of films lifted onto TEM grids (Figure S5), is proposed along with the curve. We notice that even at low surface pressure of 2 mN/m, the particles are technically not a "surface gas" state, but rather have formed patches of an incompletely organized membrane. Increasing pressure to 5 mN/m brings the "patches" together, filling the empty regions at the air/water interface and fusing them to form a uniform and incompressible film, which collapses with further pushing the pressure to 10 mN/m. Figure 2a shows the TEM image of the film lifted at 5 mN/m, where the mean particle diameter is analyzed as 1.86 ± 0.40 nm, with a uniform spacing of 1.80 nm between particle perimeters (Figure 2b). In Figure 3a we show high resolution TEM (HRTEM) images of the same sample, where we see well-defined atomic planes in the majority of the particles, indicating high crystallinity of as-prepared particles. Figure 3b is an image of even higher magnification of a typical particle, where we see that the crystal structures extend to the particle perimeter with no observable amorphous regions. From the figure we can measure the spacing between the lattice planes, $d = 0.231 \pm 0.002$ nm, from which we obtain a lattice constant of $a = 0.400$ nm, if we assume a $[1,1,1]$ orientation. This value is intermediate between lattice constants for Au and Pd metals, which are 0.408 and 0.389 nm, respectively. EDS was obtained from this sample (Figure S6), where we can see both Au and Pd peaks, from which we extracted a ratio of 2:1 for the alloy composition. Since the lattice parameters of Au and Pd are so similar, no information regarding their internal arrangement could be obtained from the images. To differentiate between a core−shell vs random alloy of the two metals, the particles were also analyzed by a "nearest neighbor" sensitive technique, known as XAS.

The data obtained from XAS are shown in Figure 4. Both the Au L_3-edge (Figure 4a) and Pd K-edge (Figure 4b) XANES spectra for AuPd resemble those for monometallic particles. In particular, Au L_3-edge XANES spectra for NP samples are qualitatively close to that of metallic foil, but with lower amplitude of XANES features, which is in agreement with the previous reports on thiol-stabilized NPs.[49] XANES spectra for Pd K-edge, in turn, differ strongly from the spectrum of Pd foil but, instead, resemble closely the XANES spectra for PdS and other species, containing the Pd−S motif.[50] Similarly, also the Pd K-edge extended X-ray absorption fine structure (EXAFS) spectra (Figure 4c,d) for both NP samples are dominated by the Pd−S contribution. In addition, a contribution of Pd−metal bonds can be observed in Fourier-transformed (FT) EXAFS spectra between 2 and 3 Å (Figure 4d) indicating that metallic Pd, or Pd−Au alloy, is also present in the sample. A strong Au−S bond contribution can also be observed in Au L_3-edge EXAFS spectra for NP samples, but in this case the contribution of the metallic bond is more evident. The contribution of Au−S bonds is stronger in the bimetallic sample than in the monometallic sample.

Best fits of experimental EXAFS spectra, obtained via the conventional procedure (see the Supporting Information) and FEFFIT code,[51] are shown in Figure 5 (for AuPd NPs) and in the Supporting Information (for monometallic particles). The obtained values of structural parameters are also reported in the Supporting Information (Table S4). As expected from visual examination of experimental data, for both monometallic and bimetallic samples quite large Au−S and, especially, Pd−S coordination numbers were obtained. Au−S and Pd−S bond
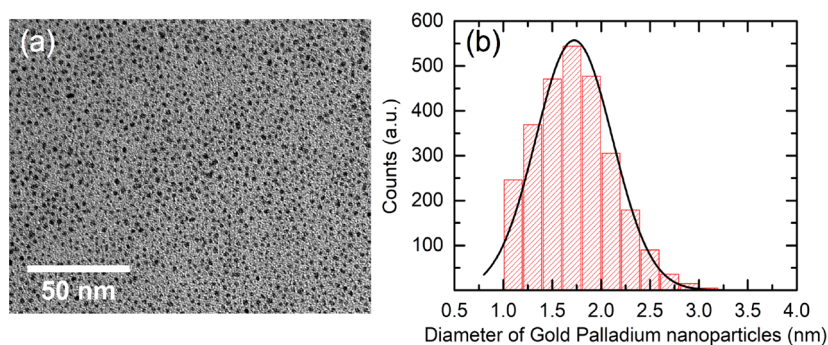
Figure 2. (a) TEM image and (b) size distribution histogram of AuPd NPs lifted at 5 mN/m.
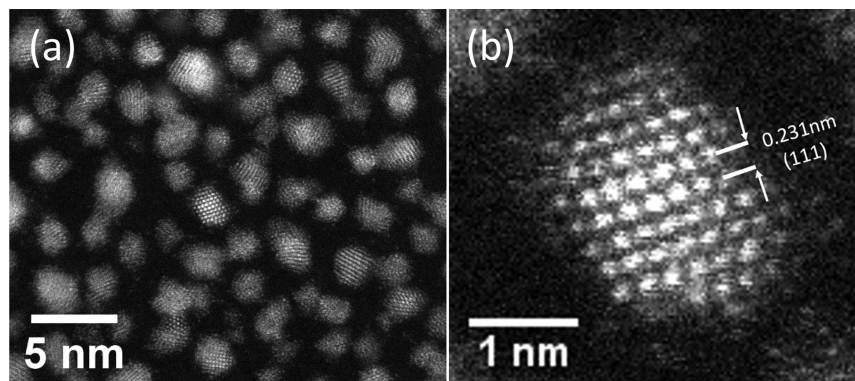

Figure 3. (a) Representative HRTEM image of AuPd NPs lifted at surface pressure of 5 mN/m. (b) Higher magnification HRTEM image with measured *d*-spacing and lattice plane of a single AuPd nanoparticle.

lengths are consistent with the previously reported ones.[52,53] Metal−metal contributions, in turn, for all samples are small and disordered, as made evident by large values of Debye−Waller factors σ^2, resulting in large error bars of our analysis. The observed low metal−metal coordination numbers and high metal−S coordination numbers indicate that the sample does not consist of monodisperse metallic NPs, covered with thiols, since such metal cores would have been much smaller than the size range observed by TEM. Therefore, similarly as in ref 53, we conclude here that the investigated samples contain two different species: metallic NPs, as well as the low molecular weight metal−thiol complexes.

Despite the fact that the distribution of metal species is heterogeneous, we obtained that the contribution of Au−Pd pairs is required for a good fit for AuPd NPs; thus we conclude that Au and Pd are alloyed in this sample. Interestingly, while the expected Au to Pd ratio in the particles is 2:1, EXAFS data suggest that, within the metallic particles, the concentration of gold is higher: the Pd−Pd coordination number is consistent with 0, while Pd−Au coordination number is approximately 2. Coordination numbers for gold also imply that metallic particles are gold-rich, but large error bars do not allow us to make quantitative analysis of segregation trends in this case. Hence the EXAFS analysis indicates that the structure of the particles is consistent with oblate particles with only Au−Au aggregates and no Pd−Pd aggregates. One possible explanation is that there is a tendency to forming an intermetallic compound composed of localized clusters or Cu_3Au structures, where the minority component is completely surrounded by the majority component, and no bonds between the minority component are formed.[54] Hence, in Au_3Pd there would be only Au−Au bonds and no Pd−Pd bonds. In our case we have

Au_2Pd (denoted as AuPd in the Article), which is similar to Au_3Pd in concentration, and the difference would be within large error bars in EXAFS coordination numbers. Hence the main result of the EXAFS analysis is the presence of alloying that is indicated by the significant contribution of Au−Pd pairs (Table S4). More accurate details on the structure and composition of AuPd particles cannot be obtained by EXAFS, due to the presence of Au−S and Pd−S species, and thus relatively small contributions of Au−metal and Pd−metal contributions to their Au and Pd EXAFS data.

The particle layer was also analyzed using X-ray reflectivity. The thickness of the layer was measured after lifting the film onto a polished and etched silicon wafer surface at the three pressures shown in Figure 6. The parameters which produced the best fitting results are tabulated in Table 1. From the table, we can see the thickness for pressures before and at the inflection point. The film has only one particle layer at the point of inflection, which is about 1.2 nm thick. The electron density of the layer corresponds to that of a solid metal having a 2:1 ratio of Au/Pd. A relatively sharp interface is established with an upper thiol layer, at the air interface, precluding any significant contribution from disordered metal/thiol complexes.

Above the inflection point, we can clearly see that the film becomes much thicker, and a second layer appears, which is nearly twice the thickness of the first one, but with the same 2:1 Au/Pd electron density, and sharp interface with a thiol layer at the air/water interface. These data indicate that, at low pressures, when the particle film is in direct contact with the aqueous phase, the particles are platelet shaped with a 2:3 ratio of thickness to diameter. As the film is compressed and rises
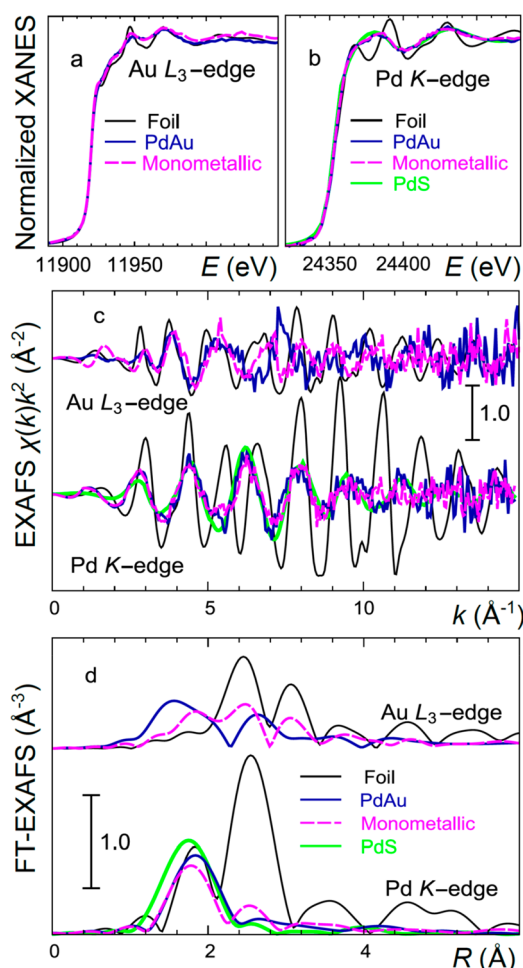
Figure 4. XANES spectra for (a) Au L_3-edge and (b) Pd K-edge in PdAu and monometallic Pd and Au samples. Corresponding (c) EXAFS spectra and (d) Fourier-transformed (FT) EXAFS spectra. Spectra for Au foil, Pd foil, and bulk PdS are shown for comparison. Spectra in parts c and d are shifted vertically for clarity.
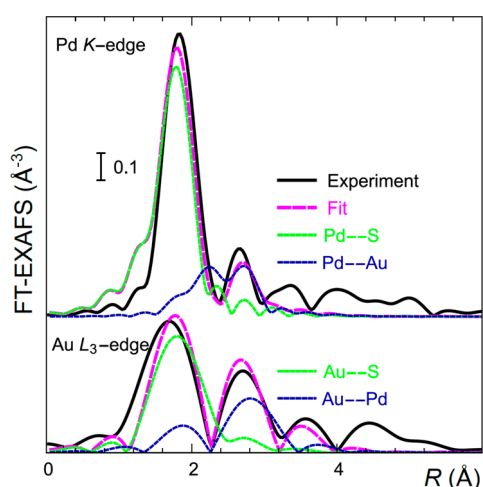

Figure 5. Fits of experimental EXAFS spectra for AuPd NP (Pd K-edge and Au L_3-edge spectra, shifted vertically for clarity). Partial contributions of Pd−S and Au−S. Pd−Au and Au−Pd are shown separately.

above the aqueous phase, the particles above the first layer are spherical again with an aspect ratio of nearly 1:1.
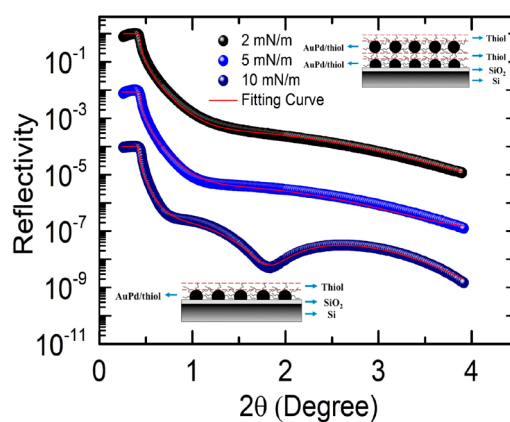

Figure 6. X-ray reflectivity measurement for AuPd NPs on silicon substrates deposited at different surface pressures: X-ray reflectivity original curve (circles) and fit curve (red line). Top insert, cartoon illustration of AuPd NP multiple layers on top of silicon wafer; bottom insert, cartoon illustration of AuPd NP monolayer on top of silicon wafer.

The platelet shape of the AuPd particles after being lifted on silicon (at the surface pressure of 5 mN/m) was also observed by cross-section TEM at high resolution (Figure S8a). Furthermore, the elemental mapping of the particles clearly shows the overlap of Au element with Pd element (Figure S8d,e), which further confirms the alloy nature of two elements in the NPs.

PEMFC Performance and Durability Assessment. We first compared the performance of the AuPd alloy monolayer to that of Au alone. Monolayers of Au and AuPd NPs were lifted onto Nafion membranes, where the coating was applied to both anode and cathode sides of the membranes, when it was lifted from the Langmuir−Blodgett (LB) trough. Polarization curves, obtained in a demonstration kit, comparable to the one used in ref 36, are shown in Figure S9a. From the figure we can see that, under ambient conditions, the power output is enhanced for both coated membranes relative to the control, with the alloy coated membrane being 17% higher than the pure Au NP coated membrane.

To determine whether the enhancement observed also translated for cells operated in the professional test station where the gas backpressure and temperature could be maintained at 150 kPa$_{abs}$ and 60 °C, respectively, an MEA was assembled by lifting AuPd particles at a pressure of 5 mN/m on a Nafion HP membrane, and the performance and durability were compared with those of an uncoated Nafion HP membrane. The performance curves are shown in (Figure 7). Several significant differences can be summarized from the curves: (1) Even though both MEAs achieved the same open circuit voltage of 0.9 V, the voltage decreases with increasing current density at a significantly larger rate in the MEA with uncoated membrane. (2) The maximum achieved current density is only 1.3 A/cm^2, as compared with 1.7 A/cm^2 of the MEA assembled with a coated membrane. (3) A 15% enhancement of the maximum power density was also witnessed by comparing the power density versus current density curves. The maximum power density achieved with the MEA assembled with a coated membrane is 0.540 W/cm^2 in contrast to 0.469 W/cm^2, measured on the MEA with uncoated membrane. (4) Furthermore, the shape of the curves broadened after applying coated membrane in MEA. It is seen

Table 1. X-ray Reflectivity Data Fitting Parameters of the Langmuir Films under Surface Pressure of 2, 5, and 10 mN/m, Where t is the Thickness, and δ is the Scattering Length Density

	2 mN/m		5 mN/m		10 mN/m	
	t (Å)	δ ($\times 10^{-5}$)	t (Å)	δ ($\times 10^{-5}$)	t (Å)	δ ($\times 10^{-5}$)
Si	N/A[a]	1.85	N/A	1.85	N/A	1.85
SiO$_2$	15	1.9	15	1.9	15	1.9
AuPd/thiol (1st)	11.5	2.09	11.6	2.27	11.8	2.85
thiol (1st)	4.5	0.41	4.6	0.45	4.86	0.42
AuPd/thiol (2nd)	N/A	N/A	N/A	N/A	21.3	1.41
thiol (2nd)	N/A	N/A	N/A	N/A	4.38	0.31

[a]N/A: not available.
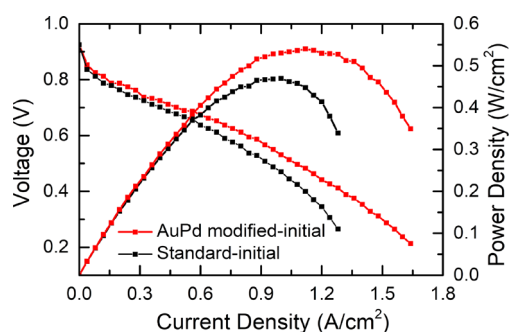
Figure 7. Polarization curve and power output of PEMFC with (red) and without (black) AuPd NP coated onto the Nafion membrane of the MEA.

that the maximum in the power density for the coated membrane one is very broad, extending from 1.1 to 1.3 A/cm^2, while peaks for the MEA with uncoated membrane are sharply located around 1.0 A/cm^2. These observations suggest that the AuPd NP coating on Nafion membrane surfaces largely promotes the initial, as well as the high current densities' performance of MEA.

To evaluate the MEAs' durability after applying our surface modified membrane, we followed the accelerated stress test (AST) cycling protocol, approved from the DOE. The polarization curves were obtained after 5K, 10K, and 15K cycles of AST (Figure S10). It is seen that the maximum current density achieved decreases with increasing of the number of cycles, reaching a maximum of 1.3 and 1.0 A/cm^2 for the MEAs with coated and uncoated membrane, respectively. The decrease in maximum power is plotted as a function of the number of cycles in Figure 8a, where we see that the variation trends of the control and the coated MEA curves are very similar, with the exception that the coated MEA one observed an enhancement of 15%, which is maintained throughout the test. More specifically (Figure 8b), the enhancement of coated membrane in voltage is amplified after 15K cycles and becomes more exaggerated at a higher current density. For instance, at current density of 0.8 A/cm^2, the voltage of the coated cell was 9% higher than that of uncoated cell initially, while it grew to 13% after 15K CV cycles. At the higher current density of 1.0 A/cm^2, the voltage of the coated cell was higher than that of the uncoated cell by 13% initially and reached 45% after 15K cycles. Hence, the advantage of the performance of an MEA resulting from the incorporation of the coated membrane is proven to last for at least 15K cycles.

Furthermore, it has also been proven that the relatively stable long-term performance of MEA could result from the
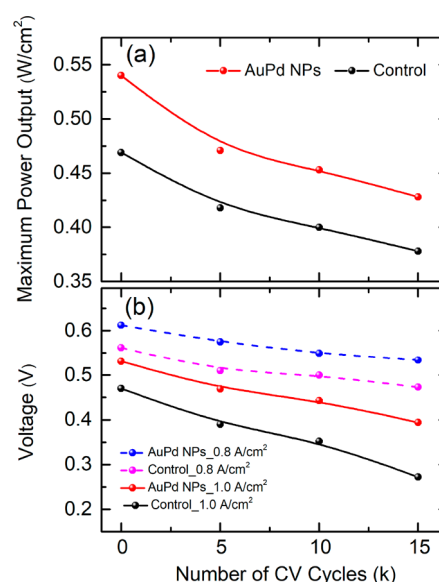

Figure 8. (a) Maximum power versus the number of CV cycles. (b) Voltage dependence of number of cycles at 0.8 and 1.0 A/cm^2 with AuPd NP coated and uncoated membrane. (The fitting curves are guides to eyes only.)

better protection of the active area of the Pt catalyst after the incorporation of the alloy particles. The initial CV curves and those obtained after 30K cycles are shown in Figure 9a for MEAs assembled with uncoated and AuPd NP coated membranes. The Pt active surface area is calculated from the area under the H$_{upd}$ adsorption peak in the CVs before and after potential cycling. For the cell operating with AuPd NPs on Nafion, the Pt active surface area decreased by 32% from 52.5 to 35.9 m^2/g after 30K CV cycles, while it decreased by 38% from 47.3 to 29.5 m^2/g after 30K CV cycles for the cell without the AuPd NPs on Nafion. The active surface area of the Pt at the electrodes is plotted as a function of the cycle number in Figure 9b. From the figure we can see that, for both MEAs, the functional forms for the decrease in area with cycle number appear similar. The largest decrease occurs after 5K cycles, and the subsequent decrease up to 30K cycles being much more gradual. Hence, despite the overall decrease in Pt surface area, the area of the Pt on the coated membrane MEAs remains 15% higher even after 30K cycles.

To explore the underlying catalytic processes responsible for the observed enhancement, we performed a series of tests on a smaller version of the MEA, which could be operated directly in air. In this test cell, the enhancement of max power output of the coated vs the uncoated membrane is magnified to nearly 60%, as shown in Figure 10b. Using this experimental set up,
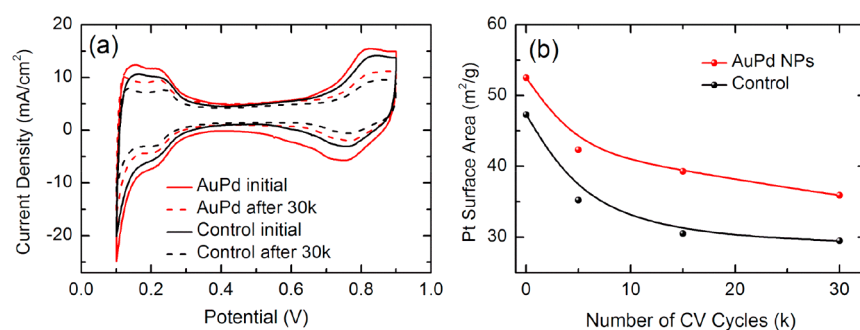
Figure 9. (a) CV curves recorded initially and after 30K CV cycles with a scan rate of 100 mV/s for cell with/without AuPd NPs on Nafion. (b) Pt surface areas calculated after different number of CV cycles. (The fitting curves are guides to eyes only.)
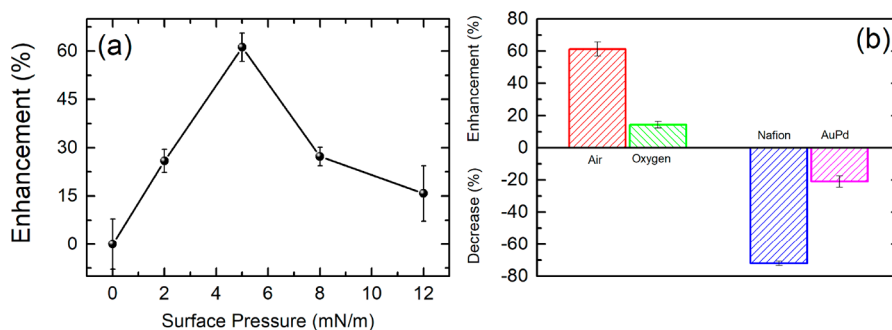

Figure 10. (a) Surface pressure dependence for the output power enhancement. (b) Comparison of power increase percentage using air or oxygen as cathode gas with AuPd NP coated Nafion and decrease percentage with/without AuPd NP coating on Nafion under mixture feed gases with 0.1% CO in hydrogen.

we obtained the polarization (Figure S9b) and power (Figure S9c) curves as a function of the surface pressure at which the particle film is deposited. The maximum power is plotted as a function of surface pressure in Figure 10a where we can see a pronounced maximum at the pressure of $P_0 = 5$ mN/m. This value corresponds to the surface pressure at the inflection point, where the incompressible monolayer (Figure S5b) is formed. Based on our previous study,[36] the significant enhancement in power output and its dependence with surface pressure might be related with the elimination of CO poisoning. The model of Haruta et al.[55] and Green et al.[56] implied that the CO oxidation reaction was catalyzed at the particle/substrate interface. Therefore, the particles had to be in direct contact with the substrate. Furthermore, the distance between particles was critical, since it had to be sufficient room for adsorption of the CO molecule, and yet the adsorbates had to be in proximity of the particle perimeter for the reaction to occur. For $P < P_0$, surface monolayer is not complete, and large empty areas could be observed in the TEM images (Figure S5a). The distance to the particles in these areas is too large, facilitating desorption. Once the layer has formed, further compression, for $P > P_0$, leads to its collapse, and as the X-ray reflectivity showed, a second layer of the particles could emerge (Figure S5c). In this case, the particles were no longer in contact with the substrate, and hence not participating in the catalytic process. In addition, since they were stacked over the membrane, they also prevented H^+ from penetration and migration from anode to cathode, which consequently reduced the current output.

The effect of different gases on the power enhancement of MEAs after applying the nanoparticles was also explored. When the cell was operated under pure oxygen at the cathode, the power output is nearly doubled for both the coated and uncoated MEAs, but the enhancement due to the alloy particle coating drops from 60% to only 15% (Figure 10b). It implies that while the electrode catalytic reaction may still be partially responsible for the enhancement, its main function at the cathode is associated with the impurity from the air (for example, CO). The largest effect was observed when 0.1% CO was mixed with the H_2 stream at the anode. The polarization curves (Figure S13b) indicate that the power output of the uncoated MEA is drastically decreased by more than 72%, whereas the power output of the coated one is decreased by only 21% (Figure 10b). The same trend was observed when 0.1% CO was introduced into the O_2 stream at the cathode (Figure S14), confirming that the AuPd particles on Nafion membrane are primarily minimizing the CO poisoning.

To theoretically describe the structure of as-prepared AuPd NPs, a model of 1.6 nm NP containing 92 atoms was built for the DFT calculation (Figure 11a). In the AuPd model, the total ratio of Au and Pd was 61:31, designed to simulate the 2:1 ratio in experiment. The shell of NP was covered by Au, considering the significant segregation of Au in AuPd alloys under reaction conditions as observed previously.[57] The core was constructed by a well-dispersed Au in Pd, since no trends of segregation of Pd atoms within AuPd NPs were detected according to the XAS measurement (Figure 11b). Following the previous study on Au NPs,[36] the low-coordinated edge and corner sites were chosen at the Nafion−AuPd interface as the active sites, and the $*SO_3$ species from Nafion was considered as the oxidizing agent for CO. Compared to Au NPs with the same size, the CO oxidation on AuPd is slightly more exothermic (-1.35 vs -1.20 eV), and the corresponding reaction barrier is lower (0.73 vs 0.79 eV); however, the transition sites in both cases are similar, which corresponds to one oxygen dissociating from $*SO_3$ and approaching $*CO$ to
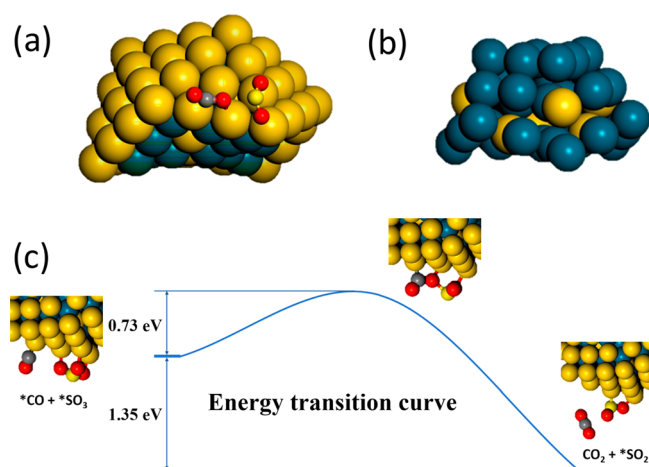
Figure 11. (a) Transition state of CO oxidation by SO_3 on AuPd NPs. (b) Core structure of AuPd NPs. (c) DFT-calculated energy transition for CO oxidation on AuPd NPs (dark yellow, Au; blue, Pd; gray, carbon; red, oxygen; light yellow, sulfur).

form $^*CO_2$ (Figure 11c). The structure, which best fits both the experiment and the DFT model for the atomic arrangement, is shown in Figure 11a, where we can see that it corresponds to a Au shell surrounding a AuPd core. This is in qualitative agreement with EXAFS results because both the DFT model and EXAFS-derived model agree that Au and Pd are well-mixed in the core of the particle. Thus, EXAFS was used to constrain the possible initial structures that could be used in DFT simulations, including, e.g., cluster-by-cluster (Au and Pd) or core–shell configurations. However, according to the DFT calculations, the nanoparticle that adopts the well-mixed AuPd bulk structure is not stable, because of the presence of Pd atoms on the shell. Instead, some Au atoms prefer to segregate from the core and form a Au-rich shell over the Au–Pd core, which are justified by prior results[57] and are beyond those structural details that could be extracted from EXAFS experiments. Alternatively, the unstable Pd atoms on the shell may also dissolute to the solution due to the strong interaction with thiols, which also results in a Au-rich shell, and it is the shell, being in contact with the membrane, that is most relevant to the catalysis.

4. CONCLUSIONS

In conclusion, we have shown that using a modified, two-phase, Brust method, AuPd alloy nanoparticles with diameter of 2.02 ± 0.56 nm can easily be synthesized. When the particles are spread at the air/water interface, they possess a distinct pressure area isotherm curve, which corresponds to monolayer and multilayer formation. X-ray reflectivity of particle layers deposited onto silicon substrates using the Langmuir–Blodgett lift-off technique indicates that initially a layer of uniform thickness, 1.16 ± 0.02 nm, is formed, where the particles become platelet-like at the air/water interface. Further compression of the layer produces another layer, twice the thickness of the first layer, suggesting that the particles resume their initial spherical shape when not at the air/water interface. High resolution TEM imaging of the monolayer indicates that the particles are highly crystalline, with well-defined atomic planes and self-assembly in an ordered hexagonal structure. EXAFS analysis of the LB lift-off films shows that only Au–Au and Au–Pd configurations were observed, indicating that the structure corresponds to that of a random alloy core surrounded by a Au shell. When the particle monolayer was lifted onto the Nafion membrane and assembled into an MEA of a PEMFC, a 15% increase in maximum power output relative to the uncoated membrane was observed, and a maximum power output of 0.540 W/cm^2 was obtained with a Pt loading of only 0.15 and 0.05 mg/cm^2 at the cathode and anode, respectively. The enhanced performance, as measured via the fuel cell test station and potentiostat, is stable and persists even after 30K cycles.

To determine the mechanism, the PEMFCs were operated using different gas mixtures. For both control and modified membrane, PEMFC performs better when oxygen was substituted for air at the cathode, but only minimal enhancement relative to the control was observed when the particle coating was applied. In contrast, when 0.1% CO was mixed either into the input H_2 stream at the anode or with O_2 at the cathode, a significant decrease of 72% and 61% in the power output at the anode and cathode, respectively, was observed in the control MEA. In contrast, PEMFCs with the particle-coated MEAs only experienced a decrease of 21% and 17% at the cathode and anode, respectively, indicating that the particles are highly effective in catalyzing the oxidation of CO. DFT calculations, using the measured particle structures, show that the SO_3 functionalities provided by Nafion membrane serve a similar function to the metal oxide supports in stretching the CO bond, facilitating oxidation. The calculations show that the activation energy barrier for the oxidation of CO at the perimeter sites of AuPd NPs is reduced to 0.73 eV, enabling the removal of CO at ambient temperatures. Hence the combination of platelet morphology in contact with the Nafion membrane succeeded in producing a new type of CO resistant PEMFCs, which could operate at lower temperatures on impure, but abundant hydrogen gas such as that produced by reformate or electrolysis processes. The availability of inexpensive H_2 opens up new opportunities for gas distribution and greatly facilitates the commercialization of PEMFCs.

■ ASSOCIATED CONTENT

Ⓢ Supporting Information

The Supporting Information is available free of charge on the ACS Publications website at DOI: 10.1021/acscatal.8b03611.

> Performance comparison; TEM, XRD, XRF, EDS, STEM characterization; details of EXAFS data fitting; and PEMFC performance curves (PDF)

■ AUTHOR INFORMATION

Corresponding Authors

*E-mail: hongfei.li@stonybrook.edu. Phone: (631) 561-3472.
*E-mail: miriam.rafailovich@stonybrook.edu. Phone: (516) 458-9011.

ORCID Ⓞ

Likun Wang: 0000-0001-9115-0220
Qiao Qiao: 0000-0002-0229-4407
Yichen Guo: 0000-0002-1637-4440
Chang-Yong Nam: 0000-0002-9093-4063
Ping Liu: 0000-0001-8363-070X
Anatoly I. Frenkel: 0000-0002-5451-1207
Yimei Zhu: 0000-0002-1638-7217

Notes

The authors declare no competing financial interest.

ACKNOWLEDGMENTS

REFERENCES

(1) Debe, M. K. Electrocatalyst Approaches and Challenges for Automotive Fuel Cells. *Nature* **2012**, *486*, 43−51.

(2) Lee, Y. M. Fuel Cells: Operating Flexibly. *Nat. Energy* **2016**, *1*, 16136.

(3) Han, B.; Carlton, C. E.; Kongkanand, A.; Kukreja, R. S.; Theobald, B. R.; Gan, L.; O'Malley, R.; Strasser, P.; Wagner, F. T.; Shao-Horn, Y. Record Activity and Stability of Dealloyed Bimetallic Catalysts for Proton Exchange Membrane Fuel Cells. *Energy Environ. Sci.* **2015**, *8*, 258−266.

(4) Chen, P.; Wang, L.-K.; Wang, G.; Gao, M.-R.; Ge, J.; Yuan, W.-J.; Shen, Y.-H.; Xie, A.-J.; Yu, S.-H. Nitrogen-Doped Nanoporous Carbon Nanosheets Derived from Plant Biomass: An Efficient Catalyst for Oxygen Reduction Reaction. *Energy Environ. Sci.* **2014**, *7*, 4095−4103.

(5) Scofield, M. E.; Zhou, Y.; Yue, S.; Wang, L.; Su, D.; Tong, X.; Vukmirovic, M. B.; Adzic, R. R.; Wong, S. S. Role of Chemical Composition in the Enhanced Catalytic Activity of Pt-Based Alloyed Ultrathin Nanowires for the Hydrogen Oxidation Reaction under Alkaline Conditions. *ACS Catal.* **2016**, *6*, 3895−3908.

(6) Zhang, J.; Sasaki, K.; Sutter, E.; Adzic, R. Stabilization of Platinum Oxygen-Reduction Electrocatalysts Using Gold Clusters. *Science* **2007**, *315*, 220−222.

(7) Zeng, Y.; Shao, Z.; Zhang, H.; Wang, Z.; Hong, S.; Yu, H.; Yi, B. Nanostructured Ultrathin Catalyst Layer Based on Open-Walled PtCo Bimetallic Nanotube Arrays for Proton Exchange Membrane Fuel Cells. *Nano Energy* **2017**, *34*, 344−355.

(8) Wang, G.; Wang, W.-h.; Wang, L.-K.; Yao, W.-T.; Yao, P.-F.; Zhu, W.-K.; Chen, P.; Wu, Q.-S. A N-, Fe-and Co-Tridoped Carbon Nanotube/Nanoporous Carbon Nanocomposite with Synergistically Enhanced Activity for Oxygen Reduction in Acidic Media. *J. Mater. Chem. A* **2015**, *3*, 17866−17873.

(9) Yuan, W.; Li, J.; Wang, L.; Chen, P.; Xie, A.; Shen, Y. Nanocomposite of N-Doped TiO2 Nanorods and Graphene as an Effective Electrocatalyst for the Oxygen Reduction Reaction. *ACS Appl. Mater. Interfaces* **2014**, *6*, 21978−21985.

(10) Baschuk, J.; Li, X. Carbon Monoxide Poisoning of Proton Exchange Membrane Fuel Cells. *Int. J. Energy Res.* **2001**, *25*, 695−713.

(11) Green, A.; Isseroff, R.; Lin, S.; Wang, L.; Rafailovich, M. Synthesis and Characterization of Iron Nanoparticles on Partially Reduced Graphene Oxide as a Cost-Effective Catalyst for Polymer Electrolyte Membrane Fuel Cells. *MRS Commun.* **2017**, *7*, 166−172.

(12) Le Canut, J.-M.; Abouatallah, R. M.; Harrington, D. A. Detection of Membrane Drying, Fuel Cell Flooding, and Anode Catalyst Poisoning on Pemfc Stacks by Electrochemical Impedance Spectroscopy. *J. Electrochem. Soc.* **2006**, *153*, A857−A864.

(13) Lu, H.; Rihko-Struckmann, L.; Sundmacher, K. Spontaneous Oscillations of Cell Voltage, Power Density, and Anode Exit Co Concentration in a Pem Fuel Cell. *Phys. Chem. Chem. Phys.* **2011**, *13*, 18179−18185.

(14) Lee, S.; Mukerjee, S.; Ticianelli, E.; McBreen, J. Electrocatalysis of Co Tolerance in Hydrogen Oxidation Reaction in Pem Fuel Cells. *Electrochim. Acta* **1999**, *44*, 3283−3293.

(15) Li, Q.; He, R.; Gao, J.-A.; Jensen, J. O.; Bjerrum, N. J. The Co Poisoning Effect in Pemfcs Operational at Temperatures up to 200 C. *J. Electrochem. Soc.* **2003**, *150*, A1599−A1605.

(16) Li, Y.; Wang, H.; Xie, L.; Liang, Y.; Hong, G.; Dai, H. Mos2 Nanoparticles Grown on Graphene: An Advanced Catalyst for the Hydrogen Evolution Reaction. *J. Am. Chem. Soc.* **2011**, *133*, 7296−7299.

(17) Cheng, S.; Logan, B. E. Sustainable and Efficient Biohydrogen Production Via Electrohydrogenesis. *Proc. Natl. Acad. Sci. U. S. A.* **2007**, *104*, 18871−18873.

(18) Choi, S. M.; Seo, M. H.; Kim, H. J.; Lim, E. J.; Kim, W. B. Effect of Polyoxometalate Amount Deposited on Pt/C Electrocatalysts for Co Tolerant Electrooxidation of H2 in Polymer Electrolyte Fuel Cells. *Int. J. Hydrogen Energy* **2010**, *35*, 6853−6862.

(19) Balasubramanian, S.; Weidner, J. W. Analysis of an Electrochemical Filter for Removing Carbon Monoxide from Reformate Hydrogen. *J. Electrochem. Soc.* **2015**, *162*, E231−E236.

(20) Qiao, B.; Liu, J.; Wang, Y.-G.; Lin, Q.; Liu, X.; Wang, A.; Li, J.; Zhang, T.; Liu, J. Highly Efficient Catalysis of Preferential Oxidation of Co in H2-Rich Stream by Gold Single-Atom Catalysts. *ACS Catal.* **2015**, *5*, 6249−6254.

(21) Chen, G.; Zhao, Y.; Fu, G.; Duchesne, P. N.; Gu, L.; Zheng, Y.; Weng, X.; Chen, M.; Zhang, P.; Pao, C.-W.; Lee, J.-F.; Zheng, N. Interfacial Effects in Iron-Nickel Hydroxide−Platinum Nanoparticles Enhance Catalytic Oxidation. *Science* **2014**, *344*, 495−499.

(22) Atrazhev, V. V.; Astakhova, T. Y.; Dmitriev, D. V.; Erikhman, N. S.; Sultanov, V. I.; Patterson, T.; Burlatsky, S. F. The Model of Stress Distribution in Polymer Electrolyte Membrane. *J. Electrochem. Soc.* **2013**, *160*, F1129−F1137.

(23) Boccuzzi, F.; Chiorino, A.; Tsubota, S.; Haruta, M. Ftir Study of Carbon Monoxide Oxidation and Scrambling at Room Temperature over Gold Supported on Zno and Tio2. 2. *J. Phys. Chem.* **1996**, *100*, 3625−3631.

(24) Huang, X.-S.; Sun, H.; Wang, L.-C.; Liu, Y.-M.; Fan, K.-N.; Cao, Y. Morphology Effects of Nanoscale Ceria on the Activity of Au/Ceo2 Catalysts for Low-Temperature Co Oxidation. *Appl. Catal., B* **2009**, *90*, 224−232.

(25) Nie, L.; Mei, D.; Xiong, H.; Peng, B.; Ren, Z.; Hernandez, X. I. P.; DeLaRiva, A.; Wang, M.; Engelhard, M. H.; Kovarik, L.; Datye, A. K.; Wang, Y. Activation of Surface Lattice Oxygen in Single-Atom Pt/Ceo2 for Low-Temperature Co Oxidation. *Science* **2017**, *358*, 1419−1423.

(26) Saavedra, J.; Whittaker, T.; Chen, Z.; Pursell, C. J.; Rioux, R. M.; Chandler, B. D. Controlling Activity and Selectivity Using Water in the Au-Catalysed Preferential Oxidation of Co in H 2. *Nat. Chem.* **2016**, *8*, 584−589.

(27) Xu, W.; Zhan, Z.; Di, L.; Zhang, X. Enhanced Activity for Co Oxidation over Pd/Al2o3 Catalysts Prepared by Atmospheric-Pressure Cold Plasma. *Catal. Today* **2015**, *256*, 148−152.

(28) Herzing, A. A.; Kiely, C. J.; Carley, A. F.; Landon, P.; Hutchings, G. J. Identification of Active Gold Nanoclusters on Iron Oxide Supports for Co Oxidation. *Science* **2008**, *321*, 1331−1335.

(29) Qiao, B.; Wang, A.; Yang, X.; Allard, L. F.; Jiang, Z.; Cui, Y.; Liu, J.; Li, J.; Zhang, T. Single-Atom Catalysis of Co Oxidation Using Pt 1/Feo X. *Nat. Chem.* **2011**, *3*, 634−641.

(30) Green, I. X.; Tang, W.; McEntee, M.; Neurock, M.; Yates, J. T., Jr Inhibition at Perimeter Sites of Au/Tio2 Oxidation Catalyst by Reactant Oxygen. *J. Am. Chem. Soc.* **2012**, *134*, 12717−12723.

(31) Green, I. X.; Tang, W.; Neurock, M.; Yates, J. T., Jr Insights into Catalytic Oxidation at the Au/Tio2 Dual Perimeter Sites. *Acc. Chem. Res.* **2014**, *47*, 805−815.

(32) Choi, K.-K.; Hosseini, N.; Kee, J.; Kim, S.-K.; Park, C.-G. Wafer Level Package of Au-Ge System Using a Ge Chemical Vapor Deposition (Cvd) Thin Film. *Appl. Surf. Sci.* **2016**, *385*, 122−129.

(33) Vallejos, S.; Stoycheva, T.; Umek, P.; Navio, C.; Snyders, R.; Bittencourt, C.; Llobet, E.; Blackman, C.; Moniz, S.; Correig, X. Au Nanoparticle-Functionalised Wo 3 Nanoneedles and Their Application in High Sensitivity Gas Sensor Devices. *Chem. Commun.* **2011**, *47*, 565−567.

(34) Zhang, X.; Shi, F.; Yu, X.; Liu, H.; Fu, Y.; Wang, Z.; Jiang, L.; Li, X. Polyelectrolyte Multilayer as Matrix for Electrochemical Deposition of Gold Clusters: Toward Super-Hydrophobic Surface. *J. Am. Chem. Soc.* **2004**, *126*, 3064−3065.

(35) Wu, S.; Yin, Z.; He, Q.; Huang, X.; Zhou, X.; Zhang, H. Electrochemical Deposition of Semiconductor Oxides on Reduced Graphene Oxide-Based Flexible, Transparent, and Conductive Electrodes. *J. Phys. Chem. C* **2010**, *114*, 11816−11821.

(36) Li, H.; Pan, C.; Zhao, S.; Liu, P.; Zhu, Y.; Rafailovich, M. H. Enhancing Performance of Pem Fuel Cells: Using the Au Nano-platelet/Nafion Interface to Enable Co Oxidation under Ambient Conditions. *J. Catal.* **2016**, *339*, 31−37.

(37) Brust, M.; Walker, M.; Bethell, D.; Schiffrin, D. J.; Whyman, R. Synthesis of Thiol-Derivatised Gold Nanoparticles in a Two-Phase Liquid-Liquid System. *J. Chem. Soc., Chem. Commun.* **1994**, *0*, 801−802.

(38) Yan, W.; Tang, Z.; Wang, L.; Wang, Q.; Yang, H.; Chen, S. Pdau Alloyed Clusters Supported by Carbon Nanosheets as Efficient Electrocatalysts for Oxygen Reduction. *Int. J. Hydrogen Energy* **2017**, *42*, 218−227.

(39) Montalti, M.; Prodi, L.; Zaccheroni, N.; Baxter, R.; Teobaldi, G.; Zerbetto, F. Kinetics of Place-Exchange Reactions of Thiols on Gold Nanoparticles. *Langmuir* **2003**, *19*, 5172−5174.

(40) Kresse, G.; Furthmüller, J. Efficient Iterative Schemes for Ab Initio Total-Energy Calculations Using a Plane-Wave Basis Set. *Phys. Rev. B: Condens. Matter Mater. Phys.* **1996**, *54*, 11169−11186.

(41) Kresse, G.; Furthmüller, J. Efficiency of Ab-Initio Total Energy Calculations for Metals and Semiconductors Using a Plane-Wave Basis Set. *Comput. Mater. Sci.* **1996**, *6*, 15−50.

(42) Kresse, G.; Hafner, J. Ab Initio Molecular Dynamics for Liquid Metals. *Phys. Rev. B: Condens. Matter Mater. Phys.* **1993**, *47*, 558−561.

(43) Kresse, G.; Hafner, J. Ab Initio Molecular Dynamics for Open-Shell Transition Metals. *Phys. Rev. B: Condens. Matter. Phys.* **1993**, *48*, 13115−13118.

(44) Kresse, G.; Hafner, J. Ab Initio Molecular-Dynamics Simulation of the Liquid-Metal−Amorphous-Semiconductor Transition in Germanium. *Phys. Rev. B: Condens. Matter Mater. Phys.* **1994**, *49*, 14251−14269.

(45) Kresse, G.; Joubert, D. From Ultrasoft Pseudopotentials to the Projector Augmented-Wave Method. *Phys. Rev. B: Condens. Matter Mater. Phys.* **1999**, *59*, 1758−1775.

(46) Blöchl, P. E. Projector Augmented-Wave Method. *Phys. Rev. B: Condens. Matter Mater. Phys.* **1994**, *50*, 17953−17979.

(47) Henkelman, G.; Uberuaga, B. P.; Jónsson, H. A Climbing Image Nudged Elastic Band Method for Finding Saddle Points and Minimum Energy Paths. *J. Chem. Phys.* **2000**, *113*, 9901−9904.

(48) Kaiser, J. W. *Structural and Catalytic Analysis of Gold-Palladium Composite Nanoalloys*; Humboldt Universität zu Berlin, 2013.

(49) Chevrier, D.; Chatt, A.; Sham, T.; Zhang, P. A Comparative Xafs Study of Gold-Thiolate Nanoparticles and Nanoclusters. *J. Phys.: Conf. Ser.* **2013**, *430*, 012029.

(50) Timoshenko, J.; Shivhare, A.; Scott, R. W. J.; Lu, D.; Frenkel, A. I. Solving Local Structure around Dopants in Metal Nanoparticles with Ab Initio Modeling of X-Ray Absorption near Edge Structure. *Phys. Chem. Chem. Phys.* **2016**, *18*, 19621−19630.

(51) Newville, M.; Ravel, B.; Haskel, D.; Rehr, J. J.; Stern, E. A.; Yacoby, Y. Analysis of Multiple-Scattering Xafs Data Using Theoretical Standards. *Phys. B* **1995**, *208−209*, 154−156.

(52) Sun, Y.; Frenkel, A. I.; White, H.; Zhang, L.; Zhu, Y.; Xu, H.; Yang, J. C.; Koga, T.; Zaitsev, V.; Rafailovich, M. H. Comparison of Decanethiolate Gold Nanoparticles Synthesized by One-Phase and Two-Phase Methods. *J. Phys. Chem. B* **2006**, *110*, 23022−23030.

(53) Sun, Y.; Frenkel, A. I.; Isseroff, R.; Shonbrun, C.; Forman, M.; Shin, K.; Koga, T.; White, H.; Zhang, L.; Zhu, Y.; Rafailovich, M. H.; Sokolov, J. C. Characterization of Palladium Nanoparticles by Using X-Ray Reflectivity, Exafs, and Electron Microscopy. *Langmuir* **2006**, *22*, 807−816.

(54) Gross, W.; Knorr, K.; Murani, A.; Buschow, K. Crystal Field Splitting of Some Rare Earth Intermetallic Compounds with Cu 3 Au Structure. *Z. Phys. B: Condens. Matter Quanta* **1980**, *37*, 123−134.

(55) Haruta, M. Gold as a Novel Catalyst in the 21st Century: Preparation, Working Mechanism and Applications. *Gold Bull.* **2004**, *37*, 27−36.

(56) Green, I. X.; Tang, W.; Neurock, M.; Yates, J. T. Spectroscopic Observation of Dual Catalytic Sites During Oxidation of Co on a Au/Tio2 Catalyst. *Science* **2011**, *333*, 736−739.

(57) Liu, H.; An, W.; Li, Y.; Frenkel, A. I.; Sasaki, K.; Koenigsmann, C.; Su, D.; Anderson, R. M.; Crooks, R. M.; Adzic, R. R. In Situ Probing of the Active Site Geometry of Ultrathin Nanowires for the Oxygen Reduction Reaction. *J. Am. Chem. Soc.* **2015**, *137*, 12597−12609.